

# Relativistic magnetic reconnection driven by a laser interacting with a micro-scale plasma slab

Longqing Yi<sup>1,2,\*</sup>, Baifei Shen<sup>3</sup>, Alexander Pukhov<sup>4</sup>, and Tünde Fülöp<sup>1</sup>

<sup>1</sup>Department of Physics, Chalmers University of Technology, 41296 Gothenburg, Sweden

<sup>2</sup>State Key Laboratory of High Field Laser Physics, Shanghai Institute of Optics and Fine Mechanics, Chinese Academy of Sciences, P.O. Box 800-211, Shanghai 201800, China

<sup>3</sup>Department of Physics, Shanghai Normal University, Shanghai, 200234, China

<sup>4</sup>Institut für Theoretische Physik I, Heinrich-Heine-Universität Düsseldorf, Düsseldorf, 40225 Germany

\*corresponding author: longqing@chalmers.se

## ABSTRACT

Magnetic reconnection is a fundamental plasma process associated with conversion of the embedded magnetic field energy into kinetic and thermal plasma energy, via bulk acceleration and Ohmic dissipation. In many high-energy astrophysical events, magnetic reconnection is invoked to explain the non-thermal signatures. However, the processes by which field energy is transferred to the plasma to power the observed emission are still not properly understood. Here, via 3D particle-in-cell simulations of a readily available (TW-mJ-class) laser interacting with a micro-scale plasma slab, we show that when the electron beams excited on both sides of the slab approach the end of the plasma structure, ultrafast relativistic magnetic reconnection occurs in a magnetically-dominated (low- $\beta$ ) plasma. The resulting efficient particle acceleration leads to the emission of relativistic electron jets with cut-off energy  $\sim 12$  MeV. The proposed scenario can significantly improve understanding of fundamental questions such as reconnection rate, field dissipation and particle acceleration in relativistic magnetic reconnection.

Many high-energy astrophysical environments are strongly magnetized, i.e. the magnetic energy per particle exceeds the rest mass energy, so that the magnetization parameter  $\sigma \equiv B_0^2/4\pi nm_e c^2 \geq 1$ , where  $B_0$  is the magnetic field strength,  $m_e$  is the electron mass,  $n$  is the plasma density, and  $c$  is the vacuum light velocity. In such environments, magnetic reconnection (MR), operating in the relativistic regime, plays a key role in the transfer of large amount of magnetic to kinetic energy via field dissipation.<sup>1-3</sup> Motivated by numerous astrophysical observations, such as high energy emission in pulsars,<sup>4</sup> cosmological gamma-ray bursts<sup>5</sup> and active galactic nuclei jets,<sup>6,7</sup> the study of relativistic MR has made rapid progress in the last few decades through analytical studies<sup>8,9</sup> as well as 2D<sup>10-13</sup> and 3D<sup>14-18</sup> particle-in-cell (PIC) simulations. However, due to difficulties in achieving the extreme magnetic energy densities that are required to observe relativistic MR in laboratory environments, previous experimental studies investigated mainly the non-relativistic regime ( $\sigma < 1$ ). These include experimental observation of MR in tokamaks<sup>19</sup> or dedicated experiments, such as MRX.<sup>20</sup>

High-intensity laser-plasma interaction<sup>21-27</sup> is a promising way to break through the relativistic limit as the energy densities that can be achieved by high-intensity laser facilities worldwide<sup>28,29</sup> are rising rapidly. These facilities provide an important platform for the study of relativistic MR and therefore attract extensive attention. In the typical laser-driven MR experiments, two neighboring plasma bubbles are created by laser-matter interaction. The opposite azimuthal magnetic fields arise due to the Biermann battery effect ( $\nabla n \times \nabla T_e$ , where  $T_e$  is the electron temperature)<sup>30</sup> and reconnect in the midplane as they are driven together by the frozen-in-flow of bulk plasma expansion. Although most of the previous studies are focused on the non-relativistic limit, it has been reported recently that relativistic MR conditions can be achieved with such a scenario in laboratory environments.<sup>31</sup>

In the laser-driven reconnection studies based on the Biermann battery effect,<sup>21-27,31-33</sup> due to the oppositely directed magnetic fields that need to be compressed together by the plasma thermal flows, the ratio of the plasma thermal and magnetic energy,  $\beta$ , is high ( $\beta > 1$ ). As a result, the plasma is not magnetically dominated and it is therefore not clear what role MR plays in terms of energy balance. Recently it has been reported that magnetically dominated MR can be achieved by a double-turn Helmholtz capacitor-coil target,<sup>34</sup> but this approach is very difficult to extend to the relativistic regime because it requires a kJ-class laser system. Thus, in spite of the remarkable progress that has been made, relativistic MR in low- $\beta$  environments ( $\beta < 1$ ), which is closely related to the interpretation of many space plasma measurements and astronomical observations,<sup>35</sup> has not been thoroughly studied.

In this paper, we propose a novel experimental setup based on the interaction of a readily available moderately intense (TW-mJ-class) laser with a micro-sized plasma slab, resulting in ultrafast relativistic MR in the low- $\beta$ -regime. By irradiating a micro-sized plasma slab with a high-intensity laser pulse, it is possible to deposit the laser energy in a very small volume, hence significantly reducing the laser energy (by at least 1-2 orders of magnitude comparing with the results reported in Ref.<sup>31</sup>) required to achieve relativistic MR regime ( $\sigma > 1$ ). Meanwhile, since the magnetic field lines are not driven by the plasma thermal flow, the magnetically-dominated regime can be accessed. Using 3D PIC simulations, a comprehensive numerical experiment is presented, which demonstrate the MR event observed in the proposed scheme have a significant effect on the whole system. It leads to fierce (0.1-TW-class) field dissipation and highly-efficient particle acceleration, which covers 20% of the total energy transition. The enormous magnetic tension gives rise to intense relativistic jets that have so far been absent in other relativistic MR studies based on laser-plasma interaction.<sup>31,36,37</sup>

Due to these features, the proposed scenario is promising to provide an important platform to study the non-thermal signatures and energy transition in relativistic MR. In addition, we present other MR signatures including quantified agyrotropy peaks in the diffusion area,<sup>38</sup> and out-of-plane quadrupole field structures.<sup>39</sup> With recent advances in laser pulse cleaning techniques<sup>40-42</sup> and micro-target manufacturing,<sup>43</sup> the proposed scenario can be straightforwardly implemented in experiments.

### Generation of relativistic jets.

A sketch of the simulation setup is shown in Fig. 1(a). A linearly polarized (in  $y$  direction) laser with normalized laser intensity  $a_0 = eE_0/m_e c \omega_0 = 5$  (intensity  $\sim 10^{19}$  W/cm<sup>2</sup>) propagates along the  $x$ -axis, where  $E_0$  is the laser amplitude,  $\omega_0 = 2\pi c/\lambda_0$  and  $\lambda_0 = 1\mu\text{m}$  are the frequency and wavelength of the laser, respectively. The laser spot size is  $4\lambda_0$  and the duration is  $15T_0$ , where  $T_0 \approx 3.3$  fs is the laser cycle. A plasma slab with thickness (in the laser-polarizing direction)  $d = 1\lambda_0$  and length (in the laser propagation direction)  $L = 20\lambda_0$  splits the laser pulse in half. The main part of the slab has an uniform density of  $20n_c$ , where  $n_c = m_e \omega_0^2/4\pi e^2$  is the critical density. At the end of the structure (coronal region, represented by the area within the blue-box framework in Fig. 1), the density drops exponentially as  $x$  increases (scale length  $l = 2\lambda_0$ ). As the laser pulse sweeps along the slab, it drives two energetic electron beams on both sides of the plasma surface.<sup>44</sup> These electron beams are typically

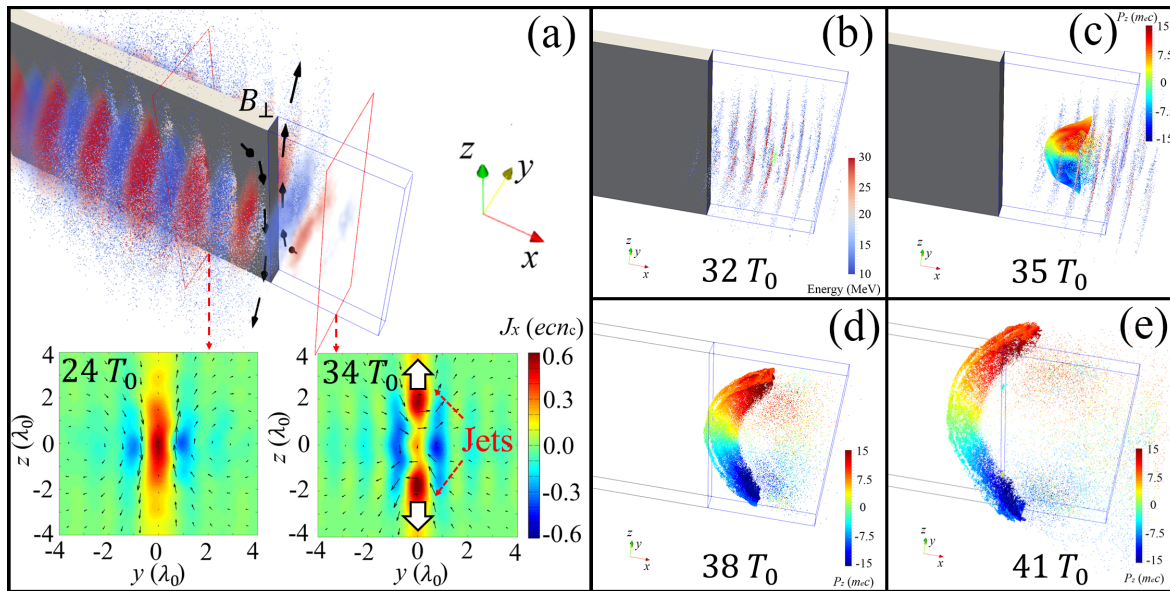


**Figure 1. Schematic of the proposed setup and relativistic jets generation.** (a) A moderately high-intensity laser pulse ( $a_0 = 5$ ) propagates along the  $x$ -direction, and is splitted in half by a micro-sized plasma slab. The laser drives two energetic electron beams on both sides of the plasma surfaces, which generates 100 MG level opposing azimuthal magnetic fields in the middle. Ultrafast magnetic reconnection is observed as the electron beams approach the coronal region (the area within the blue box, where the plasma density decreases exponentially) at the end of the slab. The two insets below show the transverse magnetic field (black arrow) and longitudinal electric current density (color) at the cross-section marked by the red rectangle (separated by  $10\lambda_0$ ) at simulation times  $t = 24T_0$  and  $t = 34T_0$ , respectively. (b-e) Generation and evolution of the relativistic jet resulting from MR at times  $32T_0$ ,  $35T_0$ ,  $38T_0$  and  $41T_0$ , respectively. The rainbow color-bar shows the transverse momentum  $P_z$  of the jets formed by the background plasma electrons and the blue-red color-bar in (b) shows the energy of the electron bunch that is driven by the laser pulse.

overdense (i.e.  $n_b > n_c$ )<sup>45</sup> and capable of generating 100 MG level opposing azimuthal magnetic fields in the middle, as shown by the black arrows in Fig. 1(a). Detailed parameters of the simulation can be found in **Methods**.

In the early stage (i.e. before the electron beams reach the corona), MR does not occur because a much stronger return current is excited inside the slab, which separates the antiparallel magnetic fields on each side of the slab, and the magnetic energy remains constant (after the initial rise due to the laser-matter interaction) during this period. As the electron beam approaches the end of the structure, the plasma density decreases rapidly so that the electron number in the local plasma becomes insufficient to form a return current that is strong enough to separate the magnetic fields. Therefore, due to Ampère's force law, the electron beams on both sides attract each other and flow into the mid-plane coronal plasma. The magnetic field lines that move with the electron beams are pushed together and reconnect. The reconnection magnetic field in the corona is approximately 100 MG. An X-point magnetic field topology is observed as shown by the right-bottom inset of Fig.1(a).

As the field topology changes, the explosive release of magnetic energy results in the emission of relativistic jets as shown by Fig. 1(b-e). These jets are formed by the background plasma electrons in the corona, which start to appear at approximately  $t = 32T_0$  [Fig. 1(b)] and acquire relativistic energies within a few laser cycles. They propagate backwards ( $-x$  direction) towards the exhaust region of the reconnection site ( $\pm z$  direction). The backward longitudinal momentum stems from efficient acceleration due to magnetic energy dissipation as will be discussed in the remainder of this work. The electrons in the jets distinguish themselves from the rest of background electrons that are heated by the laser pulse in this region by (i) remarkably higher energies (top 0.2% on the electron spectra, with mean energy  $\bar{E} \sim 4.7$  MeV), (ii) considerably small y-divergence (i.e.  $\theta_y = |P_y|/P \sim 0.1$ , where  $P$  is the electron momentum and  $P_y$  denotes its y-component), (iii) forming a dense electron beam, where the density is  $n_{jet} \sim 5n_c$  initially, but decreases rapidly due to dispersion in the  $z$ -direction. The total charge of the jets is approximately 0.2 nC.

### Pressure tensor agyrotropy and observation of field-line rearrangement.

In order to locate the reconnection site in the corona, we calculate the scalar measure of the electron pressure tensor gyrotropy that was suggested recently by Swisdak,<sup>38</sup>

$$Q = \frac{\mathcal{P}_{12}^2 + \mathcal{P}_{13}^2 + \mathcal{P}_{23}^2}{\mathcal{P}_{\perp}^2 + 2\mathcal{P}_{\perp}\mathcal{P}_{\parallel}}. \quad (1)$$

Here  $\begin{pmatrix} \mathcal{P}_{\parallel} & \mathcal{P}_{12} & \mathcal{P}_{13} \\ \mathcal{P}_{12} & \mathcal{P}_{\perp} & \mathcal{P}_{23} \\ \mathcal{P}_{13} & \mathcal{P}_{23} & \mathcal{P}_{\perp} \end{pmatrix}$  is the electron pressure tensor

$$\mathbb{P} = m \int (\mathbf{v} - \bar{\mathbf{v}})(\mathbf{v} - \bar{\mathbf{v}}) f d^3\mathbf{v} \quad (2)$$

transformed into a frame in which the diagonal components are in gyrotropic form, i.e. one of the coordinate axes points in the direction of the local magnetic field and the others are oriented such that the final two components of the diagonal of  $\mathbb{P}$  are

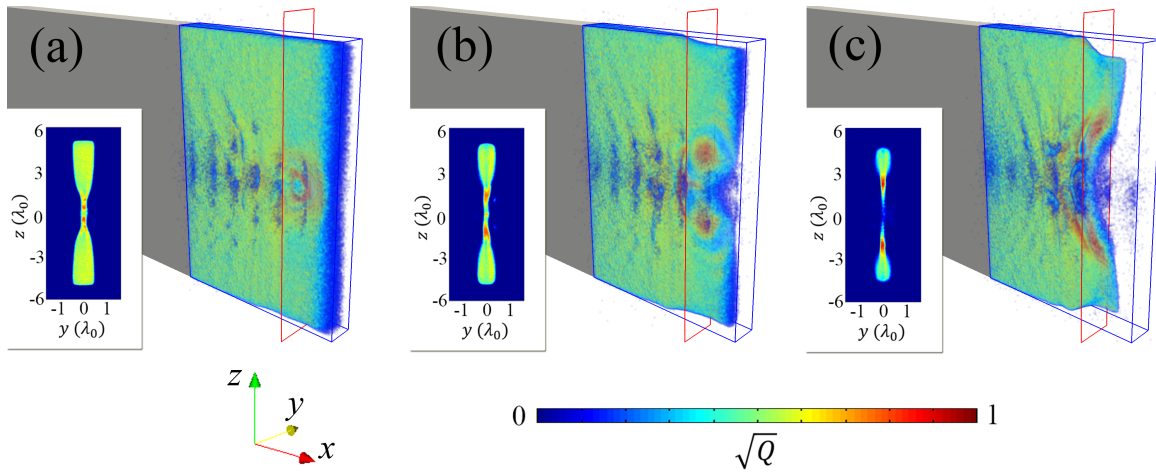


**Figure 2. Gyrotropy quantification at different times.**  $\sqrt{Q}$  in the coronal plasma at simulation time  $t = 32T_0$ (a),  $33T_0$ (b), and  $34T_0$ (c). The insets show the value of  $\sqrt{Q}$  at the cross-section with longitudinal coordinate  $x = 26\lambda_0$ , which is marked by the red rectangles in (a-c).

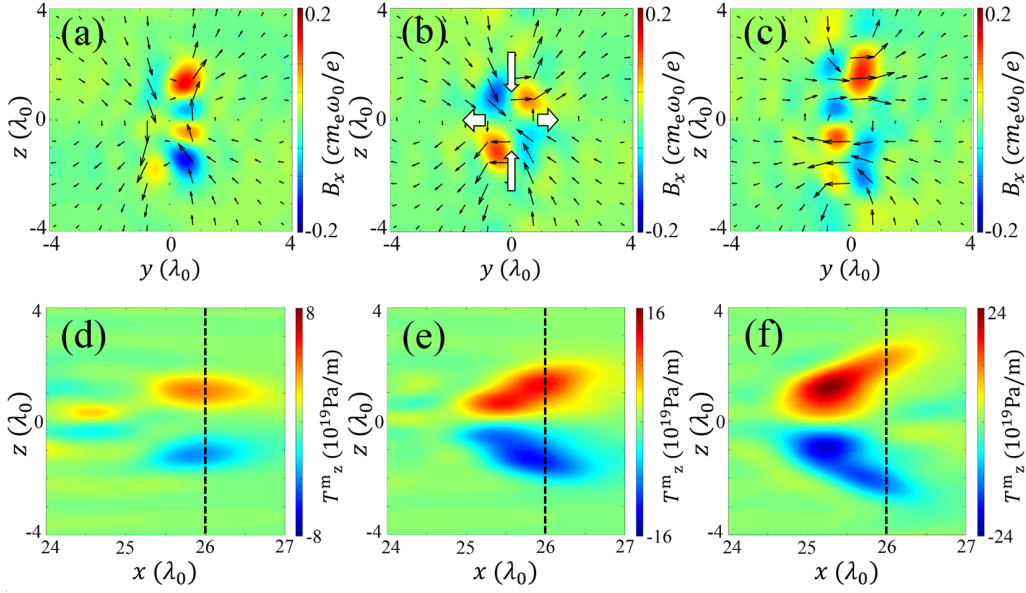


**Figure 3. Evolution of magnetic fields and magnetic tension force during the reconnection.** (a-c) Static magnetic fields (frequency below  $0.8\omega_0$ ) and (d-f)  $z$ -component of magnetic tension force at simulation time  $t = 32 T_0$  (a) & (d),  $33 T_0$  (b) & (e), and  $34 T_0$  (c) & (f). In (a-c) the transverse ( $B_y, B_z$ ) and longitudinal ( $B_x$ ) components of magnetic field are presented by the black arrows and color, respectively. The bold white arrows in (b) show the inflow (horizontal) and outflow (vertical) electric currents that result from Hall reconnection. The black-dashed lines in (d-f) mark the cross-section where the corresponding magnetic fields (a-c) are shown.

equal (see the Appendix in Ref.<sup>38</sup> for details).  $f(x, y, z, \mathbf{v})$  is the distribution function at position  $(x, y, z)$  and velocity  $(\mathbf{v})$ , and  $\bar{\mathbf{v}}$  is the mean velocity. It should be noted that although Eq. (2) is the non-relativistic definition of the electron pressure tensor, the relativistic effects are not expected to have a significant influence here since more than 99% of the electrons in the corona are non-relativistic, namely  $\gamma - 1 < 1$  as can be seen in Fig. 4(c), where  $\gamma = 1/\sqrt{1 - (v/c)^2}$  is the Lorentz factor of the electrons. In general, for gyrotropic electron pressure tensors  $Q = 0$ , and the maximum departure from gyrotropy is  $Q = 1$ . High values of  $Q$  usually identify regions of interesting magnetic topology such as separatrices and X-points in magnetic reconnection.

Figure 2 shows that the space and time where  $Q$  reaches its peak in the 3D PIC simulation coincides with the appearance of the electron jets shown in Fig. 1(b-c). The slab is significantly pinched during the interaction,<sup>46</sup> which results in a higher inflow velocity and thus a faster reconnection rate. Knowing the location of the reconnection site allows one to calculate the magnetization parameter. By substituting the electron density and magnetic field for the region with peak agyrotropy, one obtains the maximum magnetization parameter  $\sigma_m \approx 25$ . Therefore we conclude that the observed MR is in the relativistic regime.

It is generally understood that the jets are accelerated out of the reconnection region by the magnetic tension forces ( $T^m = (\mathbf{B} \cdot \nabla)\mathbf{B}/4\pi$ ) of the newly-connected, strongly-bent magnetic field lines. In Fig. 3, we plot the magnetic fields at  $x = 26\lambda_0$ , and the  $z$ -component of the magnetic tension  $T_z^m$  at the midplane ( $y = 0$ ). A quadrupole longitudinal magnetic field pattern emerges as the MR occurs, which is indicative of Hall-like reconnection,<sup>39</sup> where the reconnection rate is significantly enhanced due to decoupling of electron and ion motion. The amplitude of  $B_x$  is 20 MG, which is  $\sim 20\%$  of the reconnected magnetic field.

Figure 3 illustrates that an enormous magnetic tension force is generated in the corona because of the reconnection. The pressure exceeds the relativistic light pressure ( $P = 2I/c$  with  $a_0 \sim 1$ ) within one laser wavelength, which exerts a strong compression of the electron jets that results in the observed high-density emission. Moreover, the shape of magnetic tension in Fig. 3 shows the dynamics of the newly-connected field lines strengthening and relaxing, during which the energy is transferred to the plasma particles. The phenomenon is consistent with the shape and emission direction of the jets that we observed in Fig. 1(c-e).

### Magnetic energy dissipation and particle acceleration.

In order to gain a deeper understanding of energy transfer in the relativistic MR, we now focus on the field dissipation process. The observed dissipation power is of the order of 0.1-TW, which results in a highly efficient energy transfer from the magnetic

fields to the kinetic energy of plasma. Figure 4(a) is a graphic demonstration of 3D field dissipation, where the work done by the longitudinal electric field per unit volume and unit time (i.e.  $E_x j_x$ ) is presented. The blue chains on both sides of the slab show the process of the laser-driven electron-beams losing energy to the static electric field, which is sometimes referred to as “enhanced target normal sheath acceleration”.<sup>47</sup> Meanwhile in the midplane, one can see that the energy flows are directed in the opposite direction as MR occurs, i.e. the electrons in the coronal plasma *collectively* extract energy from the (reconnection associated) electric fields and thus gain kinetic energy. To further clarify the dissipation process, we also conducted a comparison simulation which is presented in the **Supplemental Materials**.

To further understand the role that relativistic MR plays in the energy transfer process, we calculated the energy change for each component in the simulation, i.e. laser pulse (frequency  $\geq 0.8\omega_0$ ), static electric/magnetic field (frequency  $< 0.8\omega_0$ ), and kinetic energy of electrons and protons), and the results are shown in Fig. 4(b). Let  $\Delta E_+$  denote the total energy increase in the electrostatic field, coronal electrons and protons,  $\Delta E_-$  denote the energy reduction in the laser pulse and other electrons (mostly laser-driven electron beams), and  $\Delta E_m$  represent the energy loss in the static magnetic fields. As one can see, a significant contribution to the total energy transfer comes from the annihilation of magnetic fields due to relativistic MR, which accounts for  $\sim 20\%$  of the total energy gain. Also, Fig. 4(b) indicates the static magnetic field loses  $\sim 3.0$  mJ energy in 5 laser cycles, i.e. an efficient magnetic energy dissipation with power  $\sim 0.18$  TW is obtained in the simulation. In addition, the

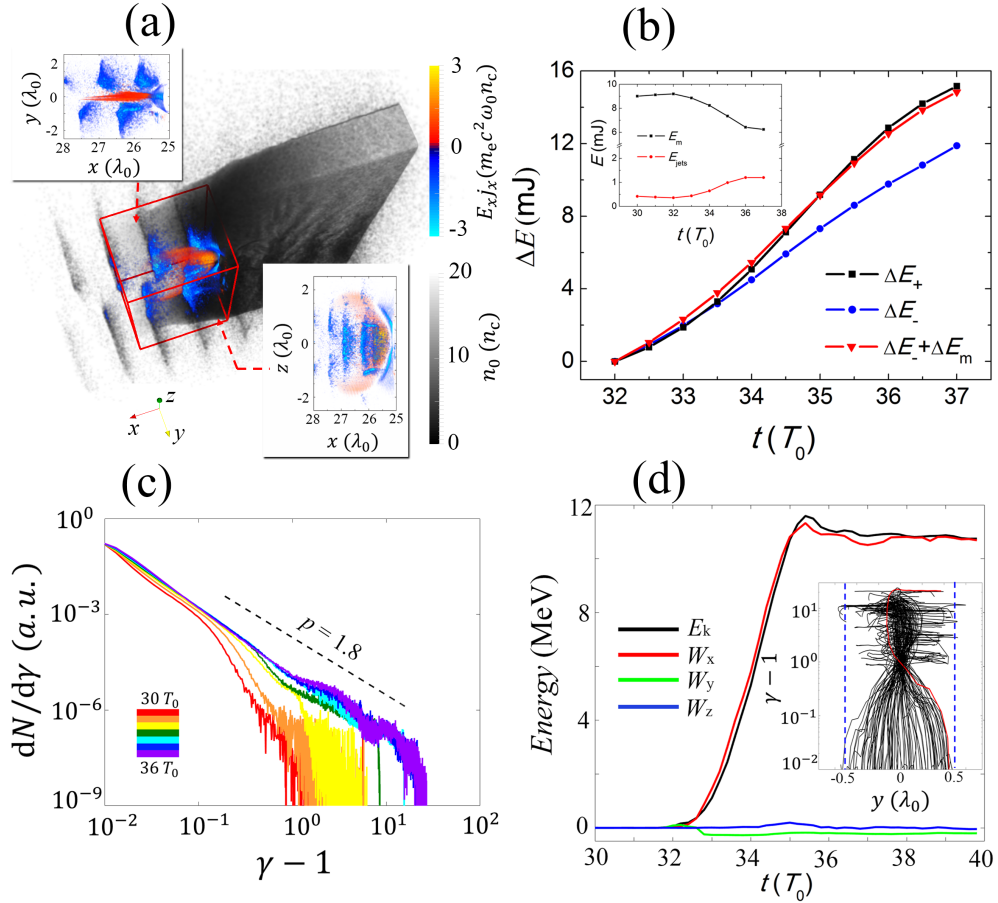


**Figure 4. Magnetic energy dissipation and the energization of non-thermal electrons.** (a) Field dissipation ( $E_x j_x$ ) and electron density at  $t = 33 T_0$  in the corona, the insets represent the top and side views of  $E_x j_x$  in the reconnection site (marked by the red box). (b) Time dependence of total energy increase in electrostatic fields, electrons in the corona, and protons ( $\Delta E_+$ ), energy reduction of electromagnetic fields and other electrons ( $\Delta E_-$ ) as well as the total energy reduction that includes magnetic field dissipation ( $\Delta E_- + \Delta E_m$ ), inset shows the evolution of static magnetic energy  $E_m$  and total kinetic energy of electron jets. (c) Coronal electron spectra from  $30 T_0$  to  $36 T_0$ . (d) The temporal evolution of the kinetic energy ( $E_k$ ) and the work done by each electric field component ( $W_x$ ,  $W_y$ , and  $W_z$ ) for one representative electron. The inset plane shows the phase-space trajectory ( $\gamma - 1$  plotted vs  $y$ ) of the total 100 tracked electrons, where the blue dashed line marks the boundary of plasma slab and the trajectory in red represents the case shown in (d).

evolution of the static magnetic energy and the kinetic energy of the electron jets are plotted in the inset of Fig. 4(b). A good time-synchronization is observed between the magnetic field dissipation and electron acceleration.

In Fig. 4(c), we plot the electron energy spectrum in the corona from  $30T_0$  to  $36T_0$ . One can see that as the reconnection occurs, the released magnetic energy is transferred to the non-thermal electrons. The total electron kinetic energy in the corona has increased by a factor of 4 during the reconnection and a hard power-law electron energy distribution  $dN/d\gamma \propto 1/\gamma^p$  is obtained with index  $p \approx 1.8$ . In addition, according to the electron energy spectrum at  $30 T_0$ , the low-energy part (with  $\gamma - 1 < 0.1$ , contains 98.8% of the total charge) has a temperature around 6 keV, given the reconnection magnetic field  $\sim 100$  MG and electron density  $\sim 1n_c$ , the plasma  $\beta$  is approximately only 0.02.

To reveal the mechanism of particle acceleration, we track 100 electrons that attain the highest energy during the MR, and display one representative case in Fig. 4(d), where the electron kinetic energy and work done by each component of the electric fields are plotted as a function of time. It illustrates that the electric field associated with reconnection at the X-point is primarily responsible for the energization of the electrons. This is supported by the trajectory of the tracked electrons in phase space [shown by the inset of Fig. 4(d), where the trajectory of the representative electron for the energy plotting is drawn in red], which shows that almost all the electrons gain their energies within a narrow plane ( $-0.1\lambda_0 < y < 0.1\lambda_0$ ) adjacent to the X-point. In this region, since the magnetic field vanishes due to the reconnection, the electrons become unmagnetized and can be accelerated freely. Moreover, as indicated by the horizontal lines in the phase space, once the electrons escape from this narrow plane, the acceleration process stops immediately. Recent studies<sup>32,33</sup> have pointed out that the randomness of the electron injection and escape from the acceleration region give rise to the observed power-law energy distribution as shown in Fig. 4(c).

### Outlook.

The present work is the first demonstration that the interaction of a high-intensity laser and a micro-scale plasma can trigger relativistic MR, which leads to highly efficient magnetic energy dissipation and gives rise to intense relativistic jets. In order to explore the potential of the proposed scenario, we conducted a series of 3D PIC simulations to study the laser intensity dependence of the maximum magnetization parameter  $\sigma_m$  and the magnetic energy dissipation  $\Delta E_m$ . The results, displayed in Fig. 5 show that, by applying a micro-sized slab target, relativistic MR can be accomplished at approximately  $a_0 = 2.5$  (where  $\sigma_m = 1.7$ ), with a laser energy of only 50 mJ. Such laser systems are readily available worldwide, which may open a way to extensive experimental study of relativistic MR and greatly advance our knowledge of the fundamental processes such as particle acceleration and magnetic energy dissipation. Moreover, as the whole setup is micro-scale, the PIC simulations are considerably less expensive than in previous laser-plasma driven MR experiments.<sup>31</sup> Since some processes of interest, such as the particle acceleration, can only be captured by means of fully-kinetic PIC simulations, it is therefore more accessible to guide and interpret future MR experiments via numerical simulations with the proposed scenario. Nevertheless, it is worth noting that despite the small physical size ( $L \sim 1 - 10\mu m$ ), due to the high energy density, in dimensionless variables<sup>48</sup> [ $L/(\sqrt{\beta}d_i) \sim 10$ , where  $d_i$  is the ion skin depth] the system here is comparable to previous laser-plasma MR experiments.

Figure 5 illustrates that as the incident laser intensity grows, the rate at which  $\sigma_m$  increases gradually slows after the initial fast-growing phase ( $3 < a_0 < 10$ ), while an opposite evolution is observed for  $\Delta E_m$ . This is because the reconnection site

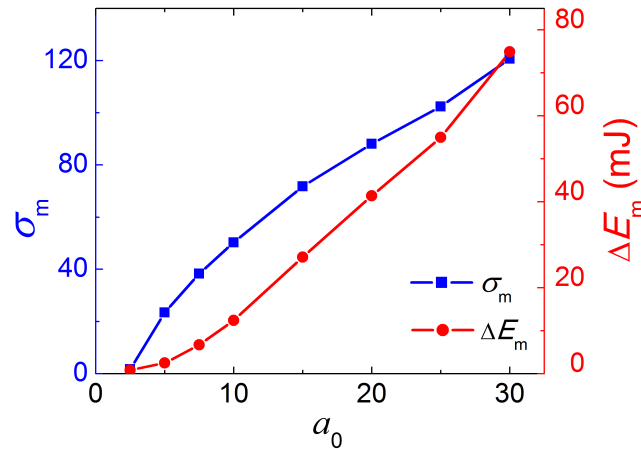


**Figure 5. Relativistic reconnection with various laser intensities.** A parameter scan showing the dependence of the maximum magnetized parameter  $\sigma_m$ , and the magnetic energy dissipation  $\Delta E_m$ , on the normalized laser amplitude  $a_0$ .

moves towards the high-density region as the laser-driven electron beams become increasingly intense, which results in stronger field dissipation (more electrons gain energy from the reconnecting field). On the other hand, the enhancement of the local plasma frequency  $\omega_p$  slows down the growth of  $\sigma_m$ . Nevertheless, it is shown that for the normalized laser amplitude  $a_0 = 30$  ( $I \sim 10^{21} \text{ W/cm}^2$ ), the regime of  $\sigma \sim 120$  can be accessed and the released magnetic energy due to field dissipation is as high as 75 mJ. With next-generation Petawatt laser facilities, such as ELI,<sup>28</sup> these results might open a new realm of possibilities for novel experimental studies of laboratory astrophysics and highly-efficient particle acceleration induced by relativistic reconnection.

## Methods

The 3D PIC simulations presented in this work were conducted with the code EPOCH.<sup>49</sup> In this study we restrict the simulations to the collisionless case, which is justified by the high temperature ( $\sim 10 \text{ keV}$ ) achieved in laser-plasma interactions, leading to particles having mean free paths larger than the system size.

A moderately high-intensity laser beam with normalized amplitude  $a_0 = 5$ , and a focus spot of  $4\lambda_0$  is used to drive the relativistic MR. The temporal profile of the laser pulse is  $T(t) = \sin^2(\pi t/\tau)$ , where  $0 \leq t \leq \tau = 15T_0$ . The power and energy of laser pulse are approximately 12 TW and 200 mJ, respectively. The plasma slab dimension is  $x \times y \times z = 20(7)\lambda_0 \times 1\lambda_0 \times 10\lambda_0$ , where the number in the bracket in  $x$  direction denotes the length of the coronal region. The slab is pre-ionized (proton-electron plasma), the initial temperature is  $T_e = T_p = 1 \text{ keV}$ . The plasma density is uniform ( $n = n_0$ ) for the main part of the slab, and decreases exponentially with  $x$  in the coronal region, i.e.  $n = n_0 \exp(-(x - x_0)^2/2l^2)$ , where  $x \geq x_0 = 21\lambda_0$  and  $l = 2\lambda_0$  is the scale length. In most of the simulations we presented in this work [except for Fig. 5],  $n_0 = 20n_c$  is applied, while in Fig. 5, we use  $n_0 = 50n_c$  for the scan runs in order to avoid problems caused by self-induced transparency at ultrahigh laser intensities. The ultra-short laser pulse duration and the relatively-low plasma density are used to improve computational efficiency, which may cause slight differences in the simulation outputs, but do not crucially alter the underlying physics of relativistic MR. For the primary simulation we presented in this work, the dimensions of the simulation box are  $x \times y \times z = 30\lambda_0 \times 15\lambda_0 \times 15\lambda_0$ , which is sampled by  $1200 \times 600 \times 600$  cells with 5 macro particles for electron species and 3 for proton species in each cell. The output of this high-resolution simulation was used to produce Fig. 1–3, and Fig. 4(a). The rest of the results presented in this work are conducted with a larger simulation box  $x \times y \times z = 40\lambda_0 \times 20\lambda_0 \times 20\lambda_0$  to ensure the laser pulse and electron beams do not leave the simulation box while we analyze the magnetic field energy, but sampled with a lower resolution  $800 \times 400 \times 400$  to reduce the computational time. The numerical convergence has been confirmed by comparing the physical quantities of interest for the simulations with different resolutions.

## Supplemental Material

Here we present a simulation with the setup depicted in Panel (a) as a comparison to the results shown in our main paper. In this setup, an additional plate is placed on the  $-y$  side of the plasma slab so that half of the laser beam is blocked. The plate thickness (in the longitudinal direction) is  $5\lambda_0$  and has the same density ( $20n_c$ ) as the slab. To ensure that the energy delivered to the corona [the volume within the blue box frame in Panel (a)] by the laser is roughly the same, we increase the laser amplitude by  $\sqrt{2}$  ( $a_0 = 7.07$ ). In this situation, only one electron beam reaches the coronal region as shown by the inset in Panel (a), and as a result the effects induced by MR are much weaker.

It should be noted that although almost all of the laser energy on the  $-y$  side of the slab is blocked by the newly-added plate, the surface current on this side is, as shown by Panel (b), not exactly zero. Therefore MR may still occur in the area with an anti-parallel magnetic field configuration [zoom-in region in Panel (b)]. However, it is found that there are significant differences that support the arguments that we made in the main paper, and are shown in Panel (c-d).

In Panel (c) we show the field dissipation ( $E_x j_x$ ) in the corona in comparison with Fig. 4(a). Obviously, the process is much stronger and significant in the 2-beam case. The reason is that the topology of the magnetic field lines are changed significantly when 2 electron beams from both sides of the slab reach the corona simultaneously. In contrast, when there is only one beam (even if it is approximately twice as intense), the collective motion of electrons, which extract energy from the collapse of magnetic fields, is almost negligible.

As a result, during the MR process, more magnetic energy is released and transferred to the plasma in the original 2-beam case, which is consistent with the analysis of electron energy in the corona, as shown in Panel (d). The total kinetic energy gain by the coronal electrons is 25% higher in the relativistic MR scenario proposed in the main paper. Moreover, we note a sharp increase of the  $E_{k,total}$  between  $32 T_0$  and  $36 T_0$  in the 2-beam case, which is in good agreement with the period during which the ultrafast relativistic MR takes place.

## References

1. Yamada, M., Kulsrud, R & Ji, H., Magnetic reconnection. *Rev. Mod. Phys.* **82**, 603 (2010).

2. Uzdensky, D. A., Magnetic reconnection in extreme astrophysical environments. *Space Sci. Rev.* **160**, 45 (2011).
3. Hoshino, M. & Lyubarsky, Y., Relativistic reconnection and particle acceleration. *Space Sci. Rev.* **173**, 521 (2012).
4. Lyubarsky Y. & Kirk J. G., Reconnection in a striped pulsar wind. *The Astrophysical Journal* **547**, 437 (2001).
5. Drenkhahn, G. & Spruit, H. C., Efficient acceleration and radiation in Poynting flux powered GRB outflows. *Astronomy & Astrophysics* **391**, 1141 (2002).
6. Romanova, M. & Lovelace, R. V. E., Magnetic field, reconnection, and particle acceleration in extragalactic jets. *Astronomy & Astrophysics* **262**, 26 (1992).
7. Matteo, T. Di, Magnetic reconnection: flares and coronal heating in active galactic nuclei. *Monthly Notices of the Royal Astronomical Society* **299**, 15 (1998).
8. Lyutikov, M. & Uzdensky, D., Dynamics of relativistic reconnection. *The Astrophysical Journal* **589**, 893 (2003).
9. Lyubarsky, Y. E., On the relativistic magnetic reconnection. *Monthly Notices of the Royal Astronomical Society* **358**, 113 (2005).
10. Drake, J. F. *et al.*, Electron acceleration from contracting magnetic islands during reconnection. *Nature* **443**, 553 (2006).
11. Zenitani, S. & Hoshino, M., Particle acceleration and field dissipation in relativistic current sheet of pair plasmas. *The Astrophysical Journal* **670**, 702 (2007).
12. Lyubarsky, Y. & Liverts, M., Particle acceleration in the driven relativistic reconnection. *The Astrophysical Journal* **682**, 1436 (2008).

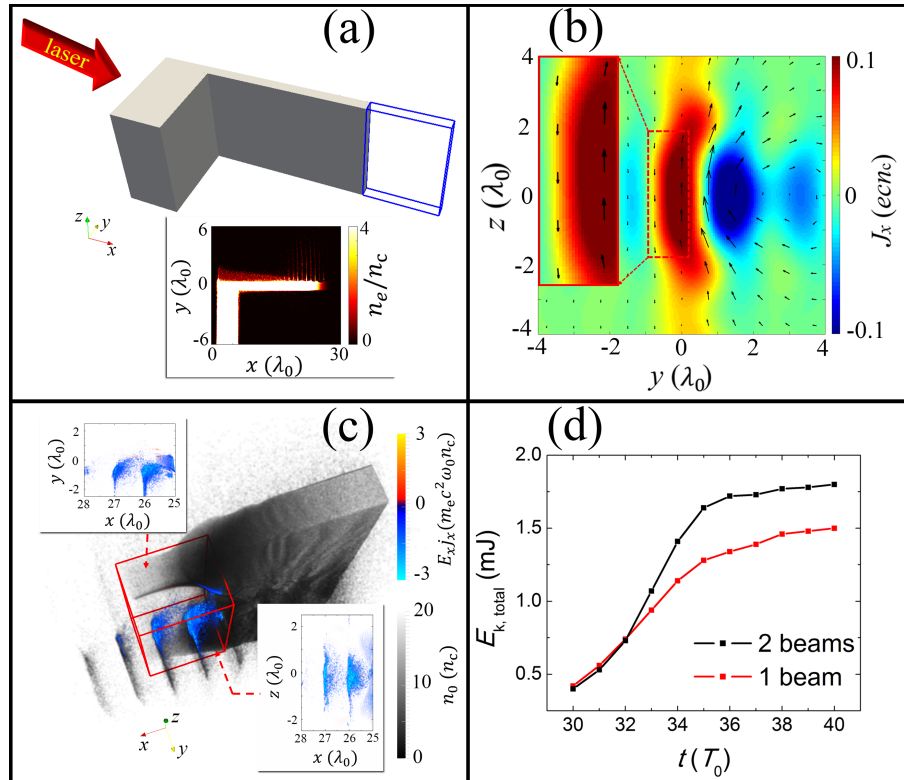


**Figure 6. Schematic and main results from the comparison simulation with one laser-driven electron beam.** (a) Sketch of the comparison simulation setup, a plate is used to block half of the laser pulse so that only one laser-driven electron beam reaches the corona (inside the blue-box). The inset shows the electron density at cross-section  $z = 0$  and simulation time  $t = 30T_0$ . (b) Longitudinal electric current density and transverse magnetic field (black arrows) at cross-section  $x = 25\lambda_0$  and  $t = 30T_0$ , the zoom-in area shows the region with anti-parallel magnetic field configuration where MR may occur. (c) Field dissipation ( $E_x j_x$ ) and electron density at  $t = 33T_0$  in the corona for the one-beam simulation. (d) Time dependence of total electron kinetic energy for one-beam (red) and two-beams (black) cases.



13. Nalewajko, K. *et al.*, On the distribution of particle acceleration sites in plasmoid-dominated relativistic magnetic reconnection. *The Astrophysical Journal* **815**, 101 (2015).
14. Sironi, L. & Spitkovsky, A., Relativistic reconnection: a efficient source of non-thermal particles. *The Astrophysical Journal* **783**, 21 (2014).
15. Guo, F. *et al.*, Formation of hard power laws in the energetic particle spectra resulting from relativistic magnetic reconnection. *Phys. Rev. Letts.* **113**, 155005 (2014).
16. Liu, W. *et al.*, Particle energization in 3D magnetic reconnection of relativistic pair plasmas. *Phys. Plasmas* **18**, 052105 (2011).
17. Kagan, D., Milosavljevic, M. & Spitkovsky, A., A flux rope network and particle acceleration in three-dimensional relativistic magnetic reconnection. *The Astrophysical Journal* **774**, 41 (2013).
18. Cerutti, B. *et al.*, Three-dimensional relativistic pair plasma reconnection with radiative feedback in the crab nebula. *The Astrophysical Journal* **782**, 104 (2014).
19. Chapman, I. T. *et al.* Magnetic reconnection triggering magnetohydrodynamic instabilities during a sawtooth crash in a tokamak plasma. *Phys. Rev. Letts.* **105**, 255002 (2010).
20. Yamada, M. *et al.*, Study of driven magnetic reconnection in a laboratory plasma. *Phys. Plasmas* **4**, 1936 (1997).
21. Nilson, P. M. *et al.*, Magnetic reconnection and plasma dynamics in two-beam laser-solid interactions. *Phys. Rev. Letts.* **97**, 255001 (2006).
22. Willingale, L. *et al.*, Proton deflectometry of a magnetic reconnection geometry. *Phys. Plasmas* **17**, 043104 (2010).
23. Zhong, J. Y. *et al.*, Modelling loop-top X-ray source and reconnection outflows in solar flares with intense lasers. *Nat. Phys.* **6**, 984 (2011).
24. Dong, Q. L. *et al.*, Plasmoid ejection and secondary current sheet generation from magnetic reconnection in laser-plasma interaction. *Phys. Rev. Letts.* **108**, 215001 (2012).
25. Fiksel, G. *et al.*, Magnetic reconnection between colliding magnetized laser-produced plasma plumes. *Phys. Rev. Letts.* **113**, 105003 (2014).
26. Rosenberg, M. J. *et al.*, A laboratory study of asymmetric magnetic reconnection in strongly driven plasmas. *Nat. Commun.* **6**, 6190 (2015).
27. Rosenberg, M. J. *et al.*, Slowing of magnetic reconnection concurrent with weakening plasma inflows and increasing collisionality in strongly driven laser-plasma experiments. *Phys. Rev. Lett.* **114**, 205004 (2015).
28. Extreme Light Infrastructure European Project, [www.eli.laser.eu](http://www.eli.laser.eu).
29. Yanovsky, V. *et al.*, Ultra-high intensity- 300-TW laser at 0.1 Hz repetition rate. *Opt. Express* **16**, 2109 (2008).
30. Stamper, J. A. *et al.*, Spontaneous magnetic fields in laser-produced plasmas. *Phys. Rev. Letts.* **26**, 1012 (1971).
31. Raymond, A. *et al.*, Relativistic Magnetic Reconnection in the Laboratory. <https://arxiv.org/abs/1610.06866> (2016).
32. Titorica S. R., Abel, T. & Fiuza, F., Nonthermal electron energization from magnetic reconnection in laser driven plasmas. *Phys. Rev. Letts.* **116**, 095003 (2016).
33. Titorica S. R., Abel, T. & Fiuza, F., Particle acceleration in laser-driven magnetic reconnection. *Phys. Plasmas* **24**, 041408 (2017).
34. Pei X. X. *et al.*, Magnetic reconnection driven by Gekko XII laser with a Helmholtz capacitor-coil target. *Phys. Plasmas* **23**, 032125 (2016).
35. Guo, F. *et al.*, Particle acceleration during magnetic reconnection in a low-beta pair plasma. *Phys. Plasmas* **23**, 055708 (2016).
36. Ping, Y. L. *et al.*, Three-dimensional fast magnetic reconnection driven by relativistic ultraintense femtosecond lasers. *Phys. Rev. E* **89**, 031101 (2014).
37. Gu, Y. J. *et al.*, Fast magnetic-field annihilation in the relativistic collisionless regime driven by two ultrashort high-intensity laser pulses. *Phys. Rev. E* **93**, 013203 (2016).
38. Swisdak, M., Quantifying gyrotropy in magnetic reconnection. *Geophys. Res. Lett.* **43**, 43 (2016).
39. Uzdensky, D. A. & Kulsrud, R. M., Physical origin of the quadrupole out-of-plane magnetic field in Hall magnetohydrodynamic reconnection. *Phys. Plasmas* **13**, 062305 (2006).

40. Jullien, A. *et al.*, Highly efficient temporal cleaner for femtosecond pulses based on cross-polarized wave generation in dual crystal scheme. *Appl. Phys. B* **84**, 409 (2006).
41. Thaury, C. *et al.*, Plasma mirrors for ultrahigh-intensity optics. *Nat. Phys.* **3**, 424 (2007).
42. Lévy, A. *et al.*, Double plasma mirror for ultrahigh temporal contrast ultraintense laser pulses. *Opt. Letts.* **32**, 310 (2007).
43. Fischer, J. & Wegener, M., Three-dimensional optical laser lithography beyond the diffraction limit. *Laser. Photon. Rev.* **7**, 22 (2013).
44. Naumova, N. *et al.*, Attosecond electron bunches. *Phys. Rev. Letts.* **93**, 195003 (2004).
45. Yi, L. *et al.*, Bright X-Ray source from a laser-driven microplasma waveguide. *Phys. Rev. Letts.* **116**, 115001 (2016).
46. Kaymak, V. *et al.*, Nanoscale ultradense Z-pinch formation from laser-irradiated nanowire arrays. *Phys. Rev. Letts.* **117**, 035004 (2016).
47. Zou, D. *et al.*, Laser-driven ion acceleration from plasma micro-channel targets. *Sci. Rep.* **7**, 42666 (2017).
48. Ji, H. & Daughton, W., Phase diagram for magnetic reconnection in heliophysical astrophysical, and laboratory plasmas. *Phys. Plasmas* **18**, 111207 (2011).
49. Arber, T. D. *et al.*, Contemporary particle-in-cell approach to laser-plasma modelling. *Plasma Phys. Control. Fusion* **57**, 113001 (2015).

## Acknowledgements

The authors would like to thank J Tenbarga, I Pusztai, S Newton, T Dubois, and the rest of the PLIONA team for fruitful discussions. This work is supported by the Knut and Alice Wallenberg Foundation, the European Research Council (ERC-2014-CoG grant 64712) and National Natural Science Foundation of China (No.11505262). The simulations were performed on resources at Chalmers Centre for Computational Science and Engineering (C3SE) provided by the Swedish National Infrastructure for Computing (SNIC).

## Author contributions statement

L.Q.Y. designed and conducted the simulations and analysed the results, under supervision of T.F.. L.Q.Y. and T.F. wrote the paper with contributions from all the coauthors.

## Additional information

Competing financial interests: The authors declare no competing financial interests.